arXiv:1608.08694v1 [astro-ph.GA] 31 Aug 2016

A Multi-Line Ammonia Survey of the Galactic Center Region with the Tsukuba 32-m Telescope – I. Observations and Data

Hitoshi ARAI,[1,2] Makoto NAGAI,[1,3] Shinji FUJITA,[1] Naomasa NAKAI,[1,3] Masumichi SETA,[1,4] Aya YAMAUCHI,[1,5] Hiroyuki KANEKO,[1,2] Kenzaburo HAGIWARA,[1] Koh-ichi MAMYODA,[1] Yusuke MIYAMOTO,[1,2] Masa-aki HORIE,[1] Shun ISHII,[1,6] Yusuke KOIDE,[1] Mitsutoshi OGINO,[1] Masaki MARUYAMA,[1] Katsuaki HIRAI,[1] Wataru OSHIRO,[1] Satoshi NAGAI,[1] Daiki AKIYAMA,[1] Keita KONAKAWA,[1] Hiroaki NONOGAWA,[1] Dragan SALAK,[1,4] Yuki TERABE,[1] Yoshiki NIHONMATSU[1] and Fumiyoshi FUNAHASHI[1]

[1]Division of Physics, Faculty of Pure and Applied Sciences, University of Tsukuba, 1-1-1 Ten-nodai, Tsukuba, Ibaraki 305-8571, Japan

[2]Nobeyama Radio Observatory, 462-2 Nobeyama, Minamimaki, Minamisaku, Nagano 384-1305, Japan

[3]Center for Integrated Research in Fundamental Science and Engineering, University of Tsukuba, 1-1-1 Ten-nodai, Tsukuba, Ibaraki 305-8571, Japan

[4]Department of Physics, School of Science and Technology, Kwansei Gakuin University, 2-1 Gakuen, Sanda, Hyogo 669-1337, Japan

[5]Mizusawa VLBI Observatory, 2-12 Hoshigaoka-cho, Mizusawa, Oshu, Iwate 023-0861, Japan

[6]Institute of Astronomy, The University of Tokyo, 2-21-1 Osawa, Mitaka, Tokyo 181-0015,

Japan

*E-mail: hitoshi.arai@nao.ac.jp

Received ; Accepted

Abstract

We present survey data of the NH_3 $(J,K)=(1,1)$–$(6,6)$ lines, simultaneously observed with the Tsukuba 32-m telescope, in the main part of the central molecular zone of the Galaxy. The total number of on-source positions was 2655. The lowest three transitions were detected with $\mathrm{S/N} > 3$ at 2323 positions (93% of all the on-source positions). Among 2323, the S/N of $(J,K)=(4,4),(5,5),$ and $(6,6)$ exceeded 3.0 at 1426 (54%), 1150 (43%), and 1359 (51%) positions, respectively. Simultaneous observations of the lines enabled us to accurately derive intensity ratios with less systematic errors. Boltzmann plots indicate there are two temperature components: cold (~ 20 K) and warm (~ 100 K). Typical intensity ratios of $T_{\rm mb}(2,2)/T_{\rm mb}(1,1)$, $T_{\rm mb}(4,4)/T_{\rm mb}(2,2)$, $T_{\rm mb}(5,5)/T_{\rm mb}(4,4)$, and $T_{\rm mb}(6,6)/T_{\rm mb}(3,3)$ were 0.71, 0.45, 0.65, and 0.17, respectively. These line ratios correspond to diversity of rotational temperature, which results from mixing of the two temperature components.

Key words: Galaxy: center – Galaxy: structure – ISM: clouds – ISM: molecules – Radio lines: ISM

1 Introduction

The central molecular zone (CMZ) of the Galaxy is a highly concentrated region of interstellar molecular gas, located within about a 200-pc radius from the Galactic Center (GC; e.g., Morris & Serabyn 1996). The molecular gas in the CMZ is characterized by the large mass ($5.3 \times 10^7 M_\odot$, Pierce-Price et al. 2000), large velocity dispersion (typical line width $\Delta v \approx$ 10–20 km s^{-1}), high number densities ($\sim 10^4$ cm^{-3}), and high temperatures. These characteristics have been shown by various molecular line observations (e.g., Jones et al. 2013) including ammonia (NH_3) inversion-lines (e.g. Hüettemeister et al. 1993). Meta-stable ($J=K$) inversion-lines of NH_3 have been often referred to as an "interstellar thermometer", because intensity ratios between the lines reflect the kinetic temperature with tiny influence of variation of the number density (e.g., Walmsley & Ungerechts 1983; Danby et al. 1988). The critical densities are not very high even at levels up to $(J,K)=(15,15)$ whose excitation energy is about 2000 K [e.g. assuming hot gas (~ 300 K), $n_{\rm H_2} \approx 10^{3\text{-}4}$ cm^{-3}, Mills & Morris 2013]. Therefore, the intensity ratios are the most reliable and powerful probe of interstellar

molecular gas temperature in very wide temperature range.

Several NH_3 observations have been made in the CMZ. First, long-scan observations along the Galactic longitude were made by Morris et al. (1983), revealing that warm temperature (rotational temperature, $T_{\rm rot} \approx 30$–60 K) is common in the region. One of the most important reports was made by Hüettemeister et al. (1993) who observed the six lowest meta-stable lines toward 36 cloud cores in the CMZ, and showed that there are two temperature components, cold and warm, in all the clouds. The cold component (~ 25 K) seems to be dense ($\sim 10^5$ cm^{-3}) and thermally coupled with dust ($T_{\rm dust}$ ≈14–20 K, Pierce-Price et al. 2000), while the warm component (> 100 K) seems to be less dense ($\sim 10^4$ cm^{-3}). Large-scale mapping observations were carried out recently by Nagayama et al. (2007, 2009) and Purcell et al. (2012). Nagayama et al. (2007, 2009) argued that the envelopes of molecular clouds are hotter than the insides and the ortho-para ratio (OPR) is high in the CMZ (∼1.5–3.5). Extremely hot NH_3 excited up to $(J, K) = (18, 18)$ was detected toward the core region of Sgr B2 as absorption lines (Wilson et al. 2006). Mills and Morris (2013) detected NH_3 $(J, K) = (8, 8)$–$(15, 15)$ lines toward 15 cloud centers, revealing that hot (over 200–300 K) molecular gas exists in various places in the CMZ. Similar warm (or hot) gas was also discovered by other line observations, such as H_2 emissions (Rodriguez-Fernandez et al. 2001), H_3^+ absorption lines (Goto et al. 2008), and H_3O^+ absorption lines (Lis et al. 2010). Their distributions, however, remain unrevealed.

Warm or hot gas is likely to be ubiquitous in the CMZ. Heating of molecular gas by dust, however, does not work in this region, because the temperature of the warm component is significantly higher than that of dust (e.g. Pierce-Price et al. 2000). Several other candidates for the heating mechanism have been proposed; mainly, (1) X-ray heating (e.g., Nagayama et al. 2007), (2) cosmic ray heating (e.g., Güsten et al. 1981; Ao et al. 2013), (3) dissipation of supersonic turbulence produced by shock phenomena (e.g., Wilson et al. 1982; Flower et al. 1995; Riquelme et al. 2013). The mechanisms (1) and (2) appear insufficient to heat the ubiquitous hot component with moderately intense X-ray (flux density, $F_X \approx 2.0 \times 10^{-3}$ erg cm^{-2} s^{-1}, Koyama et al. 2007; Ao et al. 2013) and cosmic-ray (ionization rate, $\zeta \approx$ a few 10^{-14} s^{-1}, Yusef-Zadeh et al. 2007) in the GC. On the other hand, several studies estimated that heating via shock phenomena can be attributed to the heat mechanism of molecular gas (e.g. Wilson et al. 1982; Flower et al. 1995; Mills & Morris 2013). Sources of shocks have been observationally proposed in this region so far: (1) supernova or hypernova explosions (e.g. Tanaka et al. 2009), (2) collisions between molecular clouds (Hasegawa et al. 1994; Menten et al. 2009; Mills & Morris 2013; Tsuboi et al. 2015). Collisions of molecular gas may be partly due to the barred potential of the Galaxy (Binney et al. 1991), or magnetic fields such as Parker instability (Fukui et al. 2006). To study how these shocks contribute to the heating, investigation of the distribution and morphology of warm/hot molecular gas is intrinsically important.

Table 1. Basic performance of the Tsukuba 32-m antenna of GSI.

Location	$36^\circ06'11''$ N, $140^\circ05'19''$ E
Altitude	44.6 m
Antenna mount	Cassegrain, altazimuth
Aperture diameter	32 m
Frequency bands	19.5–25.1 GHz (K-band)
Aperture efficiency	$\leq 0.41 \pm 0.02$ (at EL$\approx 38^\circ$)
Main beam efficiency	$\leq 0.49 \pm 0.02$ (at EL$\approx 38^\circ$)
Beam size	$93'' \pm 6''$ at 24.0 GHz
Polarization	right-hand circular polarization (–2009)
	right- and left-hand circular polarizations (2010–)
Backend bandwidth	1.0 GHz $\times$ 2
Spectral resolution	61 kHz

We mapped NH_3 meta-stable inversion-lines $(J,K) = (1,1)$–$(6,6)$ simultaneously in the CMZ with the Tsukuba 32-m telescope owned by the Geospatial Information Authority of Japan (GSI). In this paper, we describe observations, data analysis process, and present measured data. Detailed analysis of the data and discussion of mechanisms heating molecular clouds in the CMZ will be made in the forthcoming paper.

2 Observations and data reduction

Observations of the NH_3 $(J,K) = (1,1)$–$(6,6)$ inversion-transition lines were made over 50 days from 2009 to 2012 with the Tsukuba 32-m telescope. The basic performance of the telescope is shown in table 1. These lines were observed simultaneously. The rest frequencies and excitation energies are summarized in table 2. A radio recombination line (RRL) H64α (24.50991 GHz) was also observed at the same time. The half power beam width (HPBW) of the telescope was $93'' \pm 6''$ at 24.0 GHz, corresponding to 3.6 pc at the distance to the GC, 8.05 kpc (Honma et al. 2012). The main beam efficiency, $\eta_{\rm mb}$, of the antenna was measured by observing Jupiter whose brightness temperature was adopted to be $T_{\rm b} = 138 \pm 7$ K at 1.3 cm (23 GHz, de Pater et al. 2005). The efficiency depended on the elevation angle (EL) of the antenna as

$$\eta_{\rm mb}({\rm EL}) = 0.3337 + 7.435 \times 10^{-3}{\rm EL} - 7.159 \times 10^{-5}{\rm EL}^2 + 4.355 \times 10^{-7}{\rm EL}^3 \qquad (1)$$

at 24.0 GHz for EL $=5^\circ$–80° with the maximum value of $\eta_{\rm mb} = 0.49 \pm 0.02$ at ${\rm EL} = 38.^\circ4$.

Table 2. Properties of NH_3 rotational inversion-transitions and H64α.

Transition (J,K)	Frequency [GHz]	$E_{\rm u}/k_{\rm B}$ [K]	$a_{\rm in}/a_{\rm out}{}^*$	$v_{\rm in}/v_{\rm out}$ [km s^{-1}]†
$(1,1)$	23.694496	22.1	0.2778/0.2222	7.7/19.4
$(2,2)$	23.722633	63.3	0.0651/0.0628	16.3/26.1
$(3,3)$	23.870129	122.4	0.0300/0.0296	21.1/29.2
$(4,4)$	24.139416	199.4	0.0174/0.0173	23.7/30.9
$(5,5)$	24.532989	294.2	0.0114/0.0114	25.4/31.9
$(6,6)$	25.056025	406.9	0.0081/0.0081	26.3/32.1
H64α	24.50990‡			

* $a_{\rm in}$ and $a_{\rm out}$ are transition probabilities of the satellite lines (intensity relative to the main line in optically thin limit), which were theoretically calculated by a formula shown in the bottom of page 87 in Kukolich (1967).

† $v_{\rm in}$ and $v_{\rm out}$ are frequency offsets of the satellite lines from the main line in velocity unit, which were quoted from Simmons and Gordy (1948).

‡ Gordon and Sorochenko (2002)

The receiver front-end was a feed-horn with an ortho-mode transducer for circular polarizations, succeeded by a HEMT amplifier for each output cooled to 11 K. Right-hand circular polarization observations were started in 2009, while components for left-hand circular polarization were installed in 2010, and then dual polarizations were observed simultaneously to reduce noise level. We used two FX-type 8-bit digital spectrometers for each polarization. The bandwidth and spectral resolution of the spectrometers were 1 GHz and 61 kHz, corresponding to 12491 km s^{-1} and 0.76 km s^{-1} at 24 GHz, respectively. The spectrometers covered 23.6–24.6 GHz for $(J,K)=(1,1)$ to $(5,5)$ and 24.6–25.1 GHz for $(6,6)$, respectively.

Intensity calibration was carried out by the chopper-wheel method, yielding antenna temperature $T_{\rm A}^*$, corrected for both atmospheric and antenna ohmic losses (Ulich & Haas 1976; Kutner & Ulich 1981). The main beam brightness temperature, $T_{\rm mb}(\equiv T_{\rm A}^*/\eta_{\rm mb})$, was converted from $T_{\rm A}^*$ using the main beam efficiency $\eta_{\rm mb}$, at each observing elevation and frequency. Daily variation of the intensity scale was checked by observing Sgr B2 once a day.

During the observations, the typical system noise temperatures, $T_{\rm sys}$, were 75–200 K. Figure 1 shows the observed area. A filled circle depicted at the upper right represents the main beam size of the 32-m telescope (93″). The observations were made with the position-switching method. Reference position was $(L,B)=(1.^\circ0,-0.^\circ5)$ or $(-0.^\circ5,-0.^\circ5)$. On-source positions were on a grid with an origin of $(L,B)=(0^\circ,0^\circ)$ and at intervals of $50''$, which covered the sky with slight undersampling. The total number of on-source positions was 2655. On-source integration time was from 30 seconds to 4

Table 3. Sammary of Tsukuba 32-m NH_3 survey.

Observed lines	NH_3 $(J,K)=(1,1)$–$(6,6)$ (simultaneously)
Typical system noise temperature	75–200 K (in $T_{\rm A}^*$ scale)
Interval of grid points	$50''$ (2.0 pc at 8.05 kpc)
Total number of on-source position	2655
Effective spatial resolution	$137''$ (5.3 pc at 8.05 kpc)
Typical RMS noise level	~ 0.09 K (smoothed data in $T_{\rm mb}$ scale)

minutes, resulting in noise levels of 0.1–1.0 K for the $(1,1)$ line. To focus on spatial structure larger than the beam size, we applied spatial smoothing, described later. Pointing errors were corrected every hour by observing an H_2O maser of VX Sgr at 22.235 GHz. The typical pointing accuracy was $\sim 25''$.

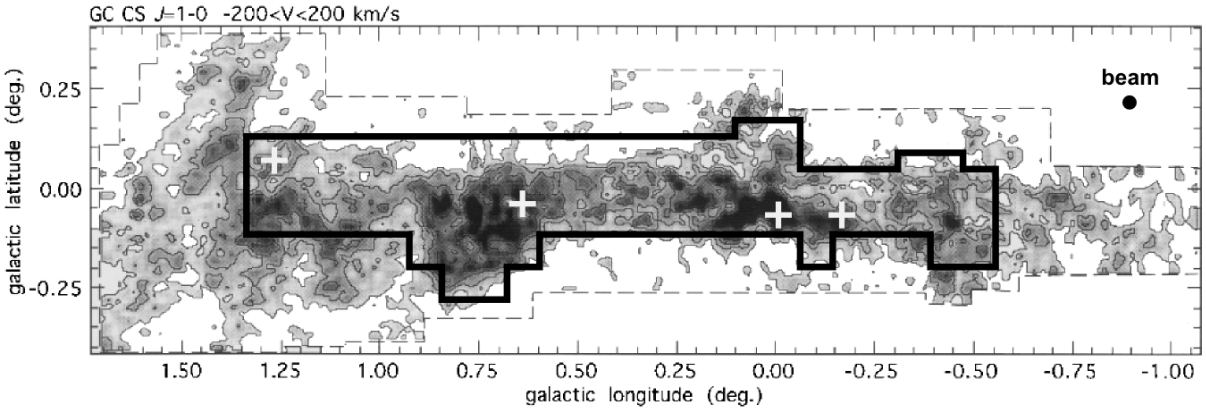

Fig. 1. Survey area surrounded by a thick line overlaid with the CS (1–0) integrated intensity map (grey scale; Tsuboi et al. 1999). The filled circle at the upper right represents the beam size of the 32-m telescope (HPBW $= 93''$). The four grey crosses indicate the positions of spectrum drawn in figure 3.

All data were reduced using the software package NEWSTAR developed by the Nobeyama Radio Observatory (NRO). We separately flagged the six NH_3 line data with bad baselines. In the $(5,5)$ and $(6,6)$, several positions lost all the data due to flagging and are dropped from the maps. The baselines of the spectra were fitted with a linear function and subtracted. The spectra were binned in the 2 km s^{-1} velocity width, sufficiently narrow compared to the typical velocity width (10–20 km s^{-1}). Then, the data cube was spatially smoothed with a Gaussian weighting function of the full width half maximum (FWHM) of $100''$, resulting in the effective spatial resolution of $\theta_{\rm Tsu} = 137''(5.3\ {\rm pc})$. After the smoothing, the noise level was reduced to typically $\Delta T_{\rm mb} \approx 0.09$ K as shown in RMS maps of figure 2.

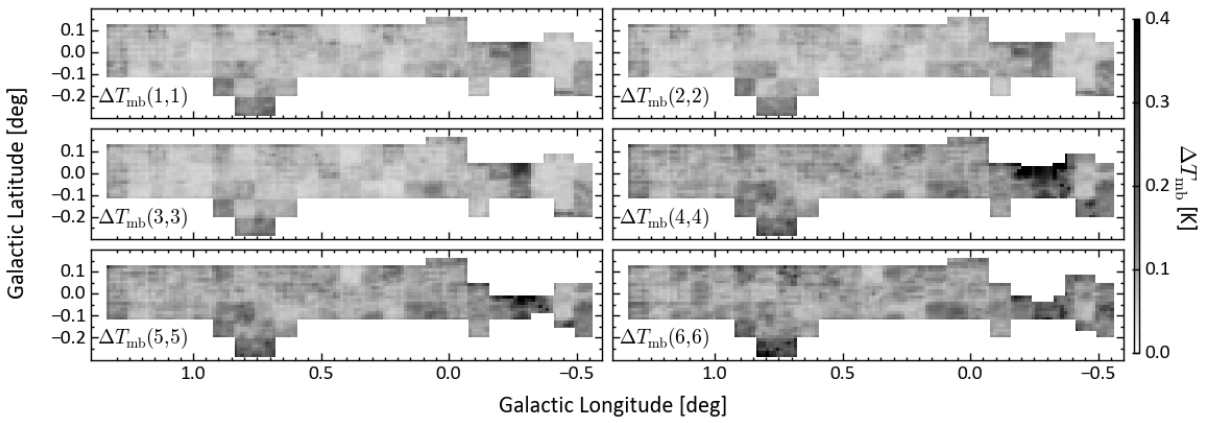

Fig. 2. RMS maps of the six NH_3 lines.

3 Results

3.1 Spectra

All signal-to-noise ratio (S/N) of the $(J,K) = (1,1)$, $(2,2)$, and $(3,3)$ lines simultaneously exceeded 3 at 2323 positions (87 % out of all observed positions). At these positions, S/N of the $(J,K) = (4,4)$, $(5,5)$, and $(6,6)$ lines exceeded 3 at 1426 (54%), 1150 (43%), and 1359 (51%) positions, respectively. The intensity of the $(3,3)$ line was the strongest at almost all observed positions and that of $(1,1)$ the second strongest. This trend was also observed in previous research efforts (e.g. Morris et al. 1983; Nagayama et al. 2009).

The NH_3 rotational-inversion lines has five groups of hyperfine lines in a narrow velocity range (< 5.5 MHz ≈ 70 km s^{-1}) [table 2; Kukolich (1967)]. They overlap with each other, however, due to their large velocity widths (≈ 20 km s^{-1}) toward the CMZ [the features of the hyperfine lines and the overlapping effect in the CMZ is well expounded by earlier studies; e.g. McGary and Ho (2002)]. Figure 3 shows sample spectra of NH_3 lines at four prominent positions "the 20–km s^{-1} cloud" (GCM$-$0.13$-$0.08), "the 50–km s^{-1} cloud" (GCM$-$0.02$-$0.07), the Sgr-B2 cloud, and the $L = 1.^{\circ}3$ region.

3.2 Distributions of Line Intensities

Figure 4 shows the spatial distributions of the integrated intensity, $I \equiv \int T_{\rm mb} dv$, of NH_3 $(J,K) = (1,1)$–$(6,6)$. Several molecular cloud complexes such as Sgr A ($L \approx 0^{\circ}$), Sgr B2 ($L \approx 0.^{\circ}7$), Sgr C ($L \approx -0.^{\circ}5$), and the $L = 1.^{\circ}3$ region can be clearly seen in all the maps. The distributions of $(J,K) = (1,1)$–$(3,3)$ lines are quite similar each other. Maps of higher transitions, $(J,K) = (4,4)$–$(6,6)$, also resemble but are more clumpy than the $(1,1)$–$(3,3)$ lines.

RRL H64α was significantly detected toward only two positions, the Sgr-B2 core region and

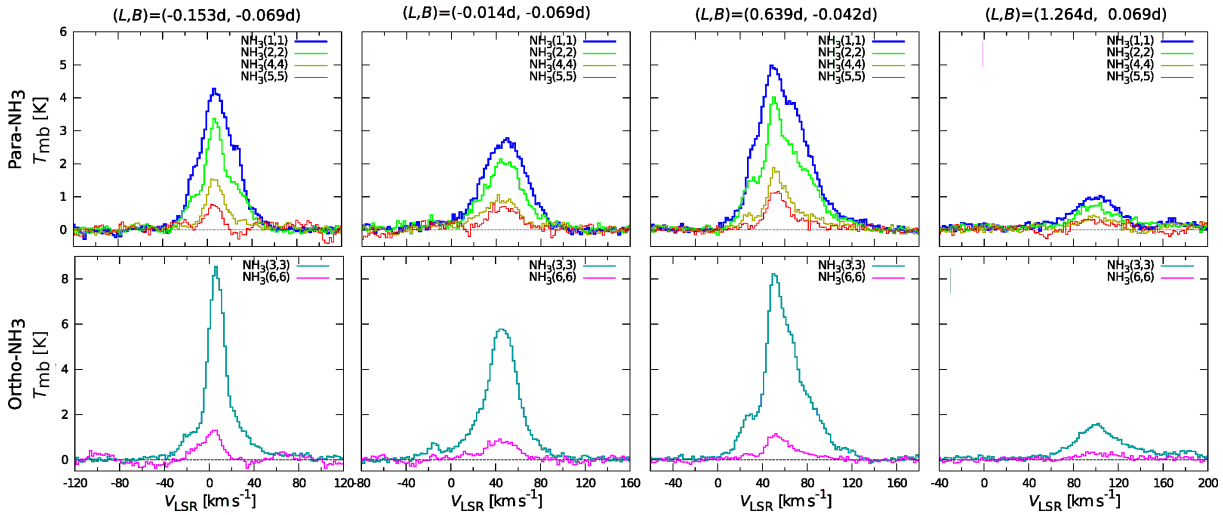

Fig. 3. Examples of NH_3 spectra at four positions. Upper panels are para-NH_3 lines and lower panels are ortho-NH_3 lines. *Left*: $(L, B) = (-0.^\circ153, -0.^\circ069)$ is in the 20-km s^{-1} cloud. *Middle left*: $(L, B) = (-0.^\circ014, -0.^\circ069)$ is in the 50-km s^{-1} cloud. *Middle right*: $(L, B) = (0.^\circ639, -0.^\circ042)$ is in the Sgr-B2 region. *Right*: $(L, B) = (1.^\circ264, 0.^\circ069)$ is in the cloud of the $1.^\circ3$ region.

the Sgr-B1 region [$(L, B) = (0.^\circ667, -0.^\circ028)$ and $(0.^\circ528, -0.^\circ056)$, with the typical $\Delta T_{\rm mb} \sim 0.13$ K]. The result is consistent with earlier research (e.g. Jones et al. 2012, 2013). Although there are several other RRLs situated close to the six NH_3 lines (e.g. H82β), they were not detected in our observed data. Therefore, the NH_3 data are not influenced by RRLs outside the two positions (i.e. the integrated intensity maps are not polluted by other than the six NH_3 lines with the exception of the Sgr-B2 core region).

Figure 5 shows the longitude-velocity diagrams with the latitude-range divided into three regions: averaged over $B = -0.^\circ285$ to $-0.^\circ118$ (left column), $B = -0.^\circ118$ to $0.^\circ049$ (center column) and $B = 0.^\circ049$ to $0.^\circ176$ (right column), respectively. The pixel size is $10'' \times 2$ km s^{-1}. No absorption due to foreground gas in the Galactic disk region was found in our NH_3 data, the same as in previous research (e.g. Nagayama et al. 2009).

3.3 Comparison with Other NH_3 Data

To verify the $T_{\rm mb}$ scaling, we compared our data with a previous survey of NH_3 $(J, K) = (1, 1)$ and $(2, 2)$ around the CMZ carried out with the Mopra 22-m telescope (Walsh et al. 2011; Purcell et al. 2012, the spatial resolution $\theta_{\rm Mop} = 2'$, data are available online). We summed the Mopra data over each 2 km s^{-1} velocity bin and smoothed them with a Gaussian function, which has the FWHM of $\sqrt{(\theta^2_{\rm Tsu} - \theta^2_{\rm Mop})} \approx 65''$ to match the spatial resolution with that of our data.

The results are shown in figure 6 as a plot of the intensity correlation between our NH_3 data and the Mopra data in the $T_{\rm mb}$ scale. The correlation is well fitted with a linear function, $T_{\rm mb}({\rm Mopra}) =$

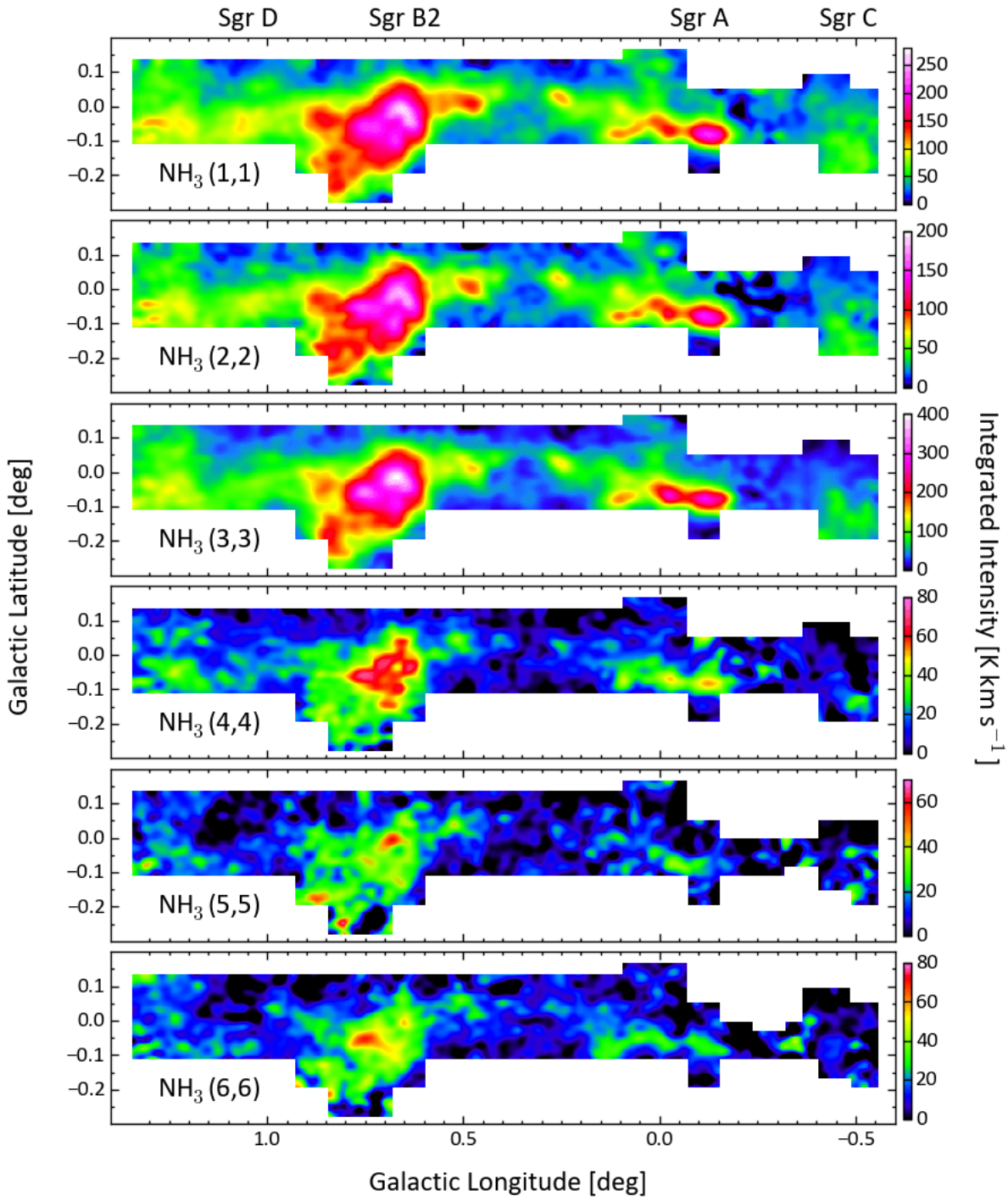

Fig. 4. Integrated intensity maps of NH_3 $(1,1)$–$(6,6)$. The integrated velocity range is $V_{\rm LSR} = -200$ to 200 km s^{-1}. These maps were spatially smoothed with a Gaussian function, resulting in the effective resolution of $137''$.

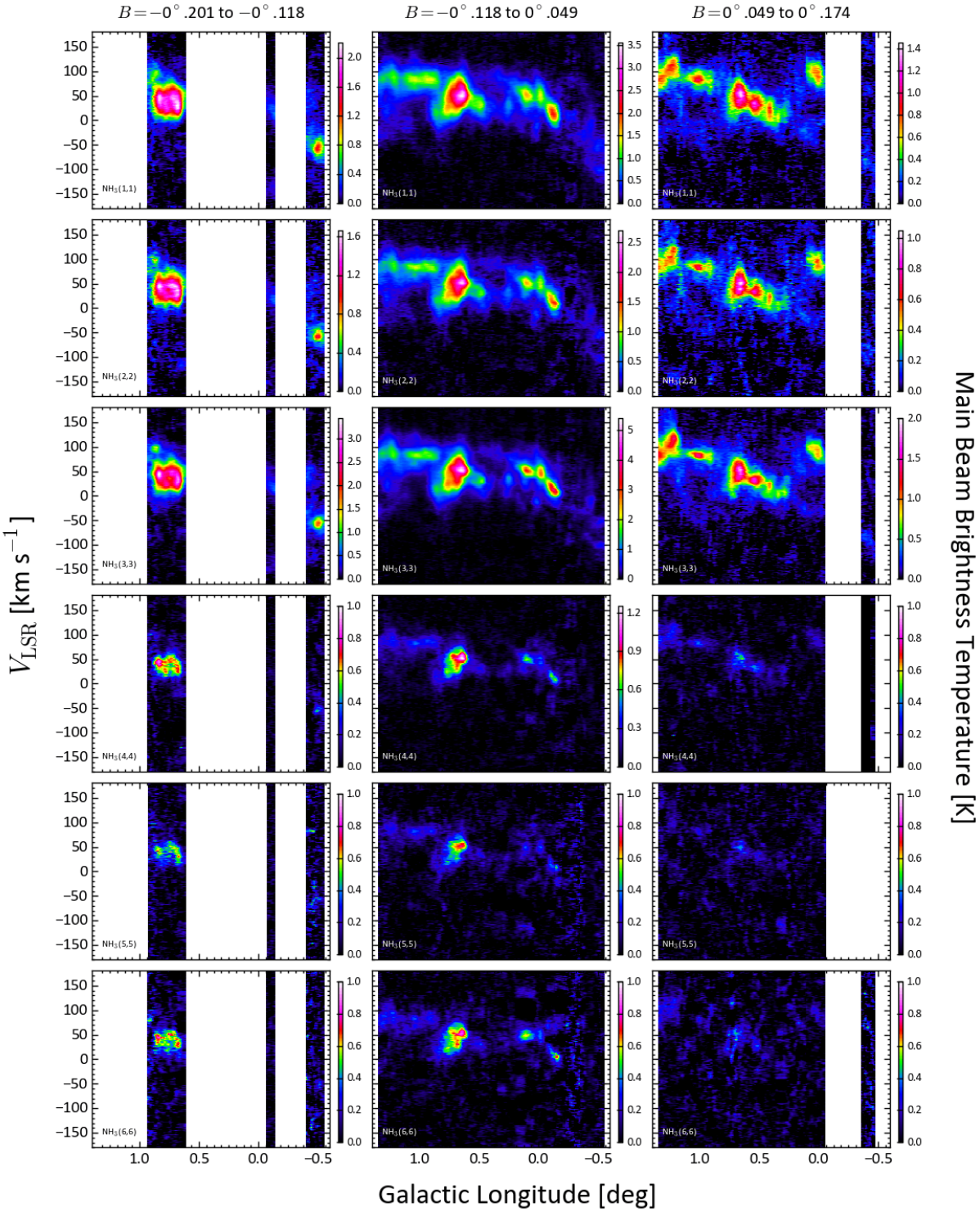

Fig. 5. The longitude-velocity diagrams of the main beam brightness temperature $T_{\rm mb}$ of NH_3 $(J,K) = (1,1)$–$(6,6)$ averaged over latitudes of $B = -0.^\circ201$–$-0.^\circ118$ (left), $B = -0.^\circ118$–$+0.^\circ049$ (center) and $B = +0.^\circ049$–$+0.^\circ174$ (right).

$0.938 \times T_{\rm mb}({\rm Tsukuba}) - 0.033$ for $(1,1)$ and $T_{\rm mb}({\rm Mopra}) = 0.944 \times T_{\rm mb}({\rm Tsukuba}) - 0.019$ for $(2,2)$, respectively, where the fitting is weighted according to the S/N of each pixel, that is, using the weight,

$$w = \left[\left(\frac{\sigma_{\rm Tsu}}{T_{\rm mb}({\rm Tsukuba})} \right)^2 + \left(\frac{\sigma_{\rm Mop}}{T_{\rm mb}({\rm Mopra})} \right)^2 \right]^{-0.5}, \quad (2)$$

where $\sigma_{\rm Tsu}$ is the noise level shown in figure 2, and $\sigma_{\rm Mop}$ is the typical noise level of the Mopra data, 0.08 K. We confirm that the difference of the $T_{\rm mb}$ scale of our data from Mopra data is less than 10%.

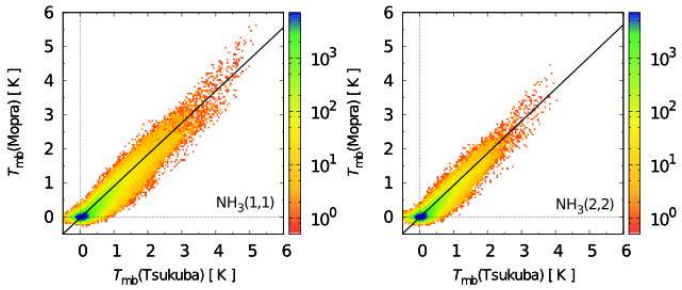

Fig. 6. Intensity correlation of the two NH_3 inversion-lines between the Tsukuba 32-m telescope and the Mopra 22-m telescope (Purcell et al. 2012). The pixel size is 0.05 K × 0.05 K. Solid lines are the result of the linear fitting; $T_{\rm mb}({\rm Mopra}) = 0.938 \times T_{\rm mb}({\rm Tsukuba}) - 0.033$ for NH_3 $(1,1)$ and $T_{\rm mb}({\rm Mopra}) = 0.944 \times T_{\rm mb}({\rm Tsukuba}) - 0.019$ for NH_3 $(2,2)$. Details are explained in subsection 3.3.

3.4 Boltzmann Plots

We can grab the excitation state with Boltzmann plots (i.e. rotational diagram, Goldsmith & Langer 1999) from multi-line observations. In a Boltzmann plot, column densities of each (J,K) normalized by the statistical weight versus the excitation energy are plotted. If a single temperature gas predominates the observed NH_3 gas, the normalized NH_3 column densities lie on a single straight slope of inverse proportion to the rotational temperature $T_{\rm rot}$.

Figure 7 shows four Boltzmann plots of our NH_3 data for the peak voxel at the same four positions as figure 3. The normalized column densities are calculated by the formula under assumptions of the local thermodynamic equilibrium (LTE) and thin optically depth

$$\frac{N(J,K)}{g(2J+1)} = \frac{3k_{\rm B}}{4\pi^3 \nu(J,K)|\mu(J,K)|^2 g(2J+1)} T_{\rm mb}(J,K)\Delta\nu, \quad (3)$$

where g is statistical weight (4 for $K = 3,6$ and 2 for the others), $k_{\rm B}$ the Boltzmann constant, $\nu(J,K)$ the line frequency, $|\mu(J,K)|^2 = \mu^2 K^2 / [J(J+1)]$, μ the permanent electric dipole moment of NH_3, 1.468 debye, $T_{\rm mb}\Delta\nu$ the integrated intensity of a voxel. Here we used a data cube of the velocity width $\Delta\nu$ smoothed to 6 km s^{-1} (i.e., the voxel size was $50'' \times 50'' \times 6$ km s^{-1}), which allows us to investigate physical conditions of each velocity component. The typical RMS noise level is about $T_{\rm mb} = 0.07$ K. Because there is satellite emission of the hyperfine splitting out of the voxel velocity

range, $N(1,1)$ is now underestimated by factor 0.5–1.0.

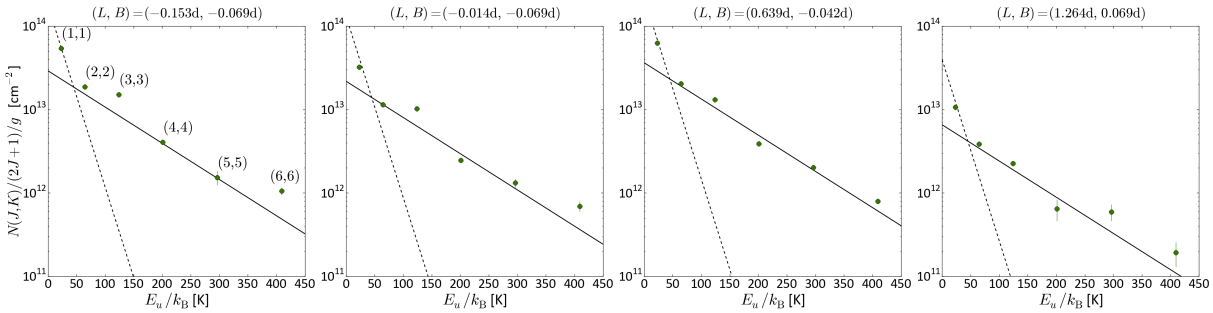

Fig. 7. Boltzmann plots of the intensity peak voxel at four points of figure 3. The velocity ranges are 3–9, 39–45, 45–51, and 87–93 km s^{-1}, respectively. Lines with a constant rotation temperature for cold (20 K, dotted) and warm (100 K, solid) are also shown as a guide. Column densities of LTE lines both cold and warm are 4×10^{14} cm^{-2}, 3×10^{14} cm^{-2}, 5×10^{14} cm^{-2} and 9×10^{13} cm^{-2}, respectively (from left to right).

The data points in figure 7 shows that populations in higher levels are warm, about 100 K; we draw a line of 100 K as a guide. Note that the ortho-NH_3 points are slightly above the line because of OPR of > 1. The points of $(1,1)$ are also above the 100–K line, indicating that there are a cold component. We draw another LTE line of 20 K whose column density is set to that of the 100–K line in each plot, which become close to the $(1,1)$ points. Hüettemeister et al. (1993) reported that the two temperature components are needed to elucidate the distribution of the NH_3 toward the cloud cores observed by them. The two temperature components are universal in our data, not only toward the cloud cores, which is shown in terms of intensity ratios in subsection 3.5. Further detailed analysis of the two temperature components including derivation of the physical state using model fitting is shown in the subsequent paper.

3.5 Intensity Ratio Distribution in Cube Data

We show distributions of the intensity ratios between two of lines: R_{21}, R_{42}, and R_{54} of para-NH_3, and R_{63} of ortho-NH_3, where $R_{ul} \equiv T_{\rm mb}(u,u)/T_{\rm mb}(l,l)$ at each voxel same as subsection 3.4 (i.e., $50'' \times 50'' \times 6$ km s^{-1}). The intensity ratios are important as the simplest indicator of molecular gas temperature, doing not involve complex derivation of physical parameters. The ratios in this subsection were calculated only at voxels where emission of the lower transition was detected over 5σ.

Figure 8 shows the histograms of the intensity ratios where the ordinate is the summation of the integrated intensity of the lower transition, $T_{\rm mb}(l,l)\Delta\nu$. When the lines are optically thin, intensity ratios reflect the physical condition of gas, especially the kinetic temperature. We take the value of the peak in the histograms as a typical value (TV) of each intensity ratio. Here, we define two ranges in the histograms to characterize the distributions of the intensity ratios: predominant ratio range (PR)

Table 4. Summary of intensity ratios and corresponding rotational temperatures

	Typical ratio ($T_{\rm rot}$)	Predominant ratio range ($T_{\rm rot}$)	Higher ratio range ($T_{\rm rot}$)
R_{21}	0.71 (36 K)	0.64–0.74 (33–38 K)	> 0.86 (> 43 K)
R_{42}	0.45 (86 K)	0.40–0.50 (80–92 K)	> 0.60 (> 105 K)
R_{54}	0.65 (138 K)	0.57–0.72 (116–163 K)	> 0.96 (> 320 K)
R_{63}	0.17 (111 K)	0.14–0.20 (103–119 K)	> 0.36 (> 157 K)

and higher ratio range (HR). PR is the range collecting the largest $T_{\rm mb}(l,l)$ bins so that 40% of the total integrated intensity of the lower line is included in. HR is the range collecting the highest ratio bins including 5% of the intensity. PR and HR are filled with green and pink in figure 8. These values are summarized in table 4. The TV of R_{21} (0.71) is very close to the mean value of R_{21} reported in earlier studies (~ 0.70, Nagayama et al. 2009).

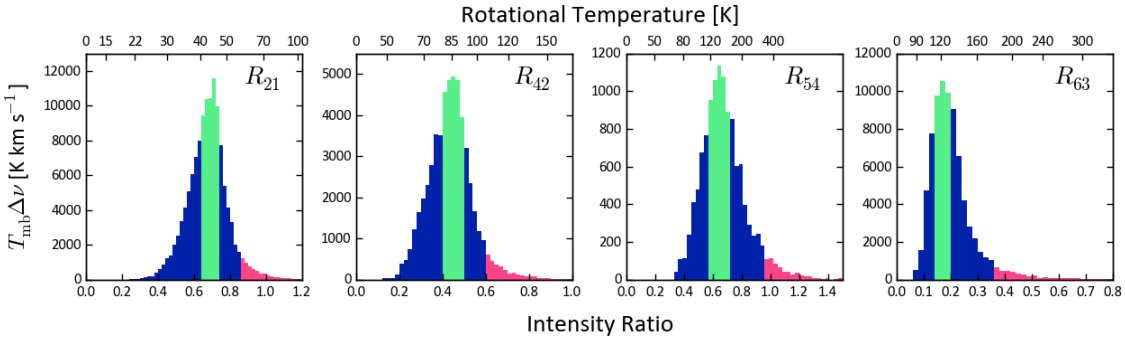

Fig. 8. Histograms of the intensity ratios, $R_{ul} \equiv T_{\rm mb}(u,u)/T_{\rm mb}(l,l)$, weighted by the integrated intensities of the lower transitions, that is, the ordinate is the summation of the integrated intensities of the lower transition, $T_{\rm mb}(l,l)\Delta\nu$. The width of the bins is $\Delta R = 0.02$. In each histogram, the predominant ratio range (PR) and the higher ratio range (HR) are indicated by light green and pink, respectively.

From the intensity ratios, we derived the corresponding rotational temperatures, T_{ul}, using the Boltzmann equation under assumptions of thin optical depths, same beam filling factors, and LTE,

$$\frac{T_{\rm mb}(u,u)}{T_{\rm mb}(l,l)} = \frac{\nu(u,u)S(u,u)}{\nu(l,l)S(l,l)} \exp\left(-\frac{\Delta E_{ul}}{k_{\rm B}T_{ul}}\right) \tag{4}$$

where $S(J,K) = (2J+1)K^2/[J(J+1)]$, and ΔE_{ul} is the energy difference between level u and l. Table 4 shows the resultant rotational temperatures. The differences among the rotational temperatures are mainly due to co-existence of two temperature components shown in subsection 3.4. The cold component has substantial contributions to the emission of $T_{\rm mb}(1,1)$, and little contributions to the emission of the other higher transitions over $T_{\rm mb}(3,3)$. Therefore, the rotational temperature T_{21} indicates the temperature of the cold gas component, and T_{54} and T_{63} indicate that of the warm (or

hot). T_{42} is contributed from both cold and warm gas components.

Figure 9 shows the distributions of the intensity ratio in the longitude-latitude (LB) map and the longitude-velocity (LV) diagram. To project 3-D voxel data to 2-D maps or diagrams, we calculated the integrated intensity ratio $\overline{R_{ul}}$ along the velocity axis or the galactic latitude axis. They are expressed as

$$\overline{R_{ul}(L,B)} = \sum_v T_{\rm mb}(u,u)(L,B,v)\Delta v \Big/ \sum_v T_{\rm mb}(l,l)(L,B,v)\Delta v, \tag{5}$$

and for LV diagrams,

$$\overline{R_{ul}(L,v)} = \sum_B T_{\rm mb}(u,u)(L,B,v)\Delta v \Big/ \sum_B T_{\rm mb}(l,l)(L,B,v)\Delta v, \tag{6}$$

where Δv and ΔB are the width of the 3-D voxel along the velocity axis and the galactic-latitude axis, respectively. The LB maps are overlaid with contours of the integrated intensities of $T_{\rm mb}(2,2)$ and the LV diagrams are overlaid with contours of $T_{\rm mb}(2,2)$ averaged along B. The inversion-lines of NH_3 have satellite lines with different apparent velocities (frequencies) from the main lines, and they would affect the intensity ratios at higher and lower frequencies (the edges of the spectrum) in the average calculation. For highly excited NH_3 transition lines, however, the effect can be ignored in the calculations, because the intensity of satellite lines is quite weak compared with that of the main line (see table 2). The most noticeable feature in the LB maps of figure 9 is the distribution of $\overline{R_{63}}$, namely the intensity ratio is higher at outer parts of giant molecular clouds (GMCs) than at inner parts and a temperature gradient of warm component gas can be seen. This trend is also seen in the LV-diagram: a higher ratio is located at the velocity edges of GMCs. Since the velocity dispersion of the outer envelope of a molecular cloud tends to be larger than that of the interior (e.g. Sakamoto & Sunada 2003), the results indicate that GMCs in this region are heated from the outside of the clouds and the outer envelope becomes hotter than the inside. Detailed analysis will be shown in a forthcoming paper. Although the higher ratio at the velocity edges is also seen in the LV-diagram of R_{21}, we suspect that this is artificially caused by the substantial difference of apparent velocities of the hyperfine lines; 19.3 km s^{-1} for $(1,1)$ and 25.7 km s^{-1} for $(2,2)$.

Figure 10 shows integrated intensity maps of the lower transitions $T_{\rm mb}(l,l)$ of the four intensity ratios using only voxels in the HR (i.e., voxel with $R_{21}>0.86$, $R_{42}>0.60$, $R_{54}>0.96$, and $R_{63}>0.36$). These maps look quite different from one another. We consider that this is mainly due to the difference of contribution of cold gas component and R_{54} is the most reliable indicator of warm gas tracer because of the highest excitation energy of the lower transition. The bright region in the R_{54} map in figure 10 indicates regions where extremely high-temperature ($T_{\rm rot} > 300$ K) molecular gas exists. For example, there is a bright region in the south of the Sgr-B2 region, at $(L,B) = (0.^\circ69, -0.^\circ15)$.

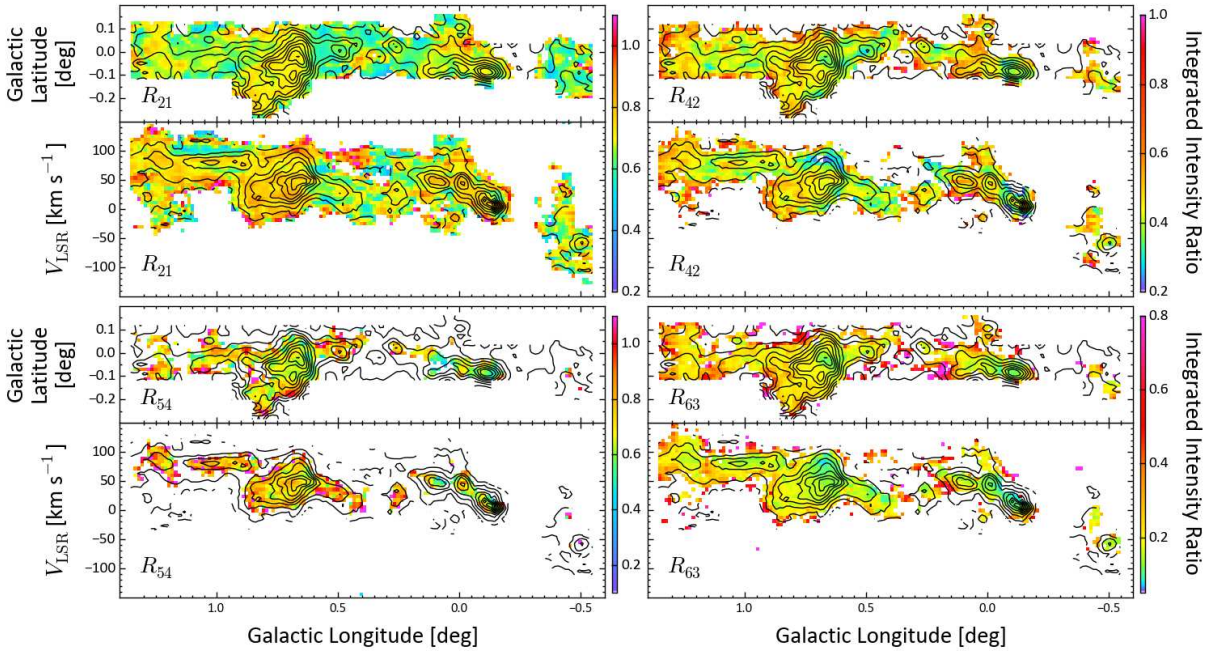

Fig. 9. Distributions of the intensity ratio, $\overline{R_{ul}}$ (color), overlaid on the distributions of the intensity of the $(J, K) = (2, 2)$ (contours). LB-maps and LV-diagrams are shown alongside. The contour interval is 18 K km s^{-1} for LB-maps and 0.2 K for LV-diagram.

This is fairly close to the region where Tsuboi et al. (2015) argued a cloud-collision event.

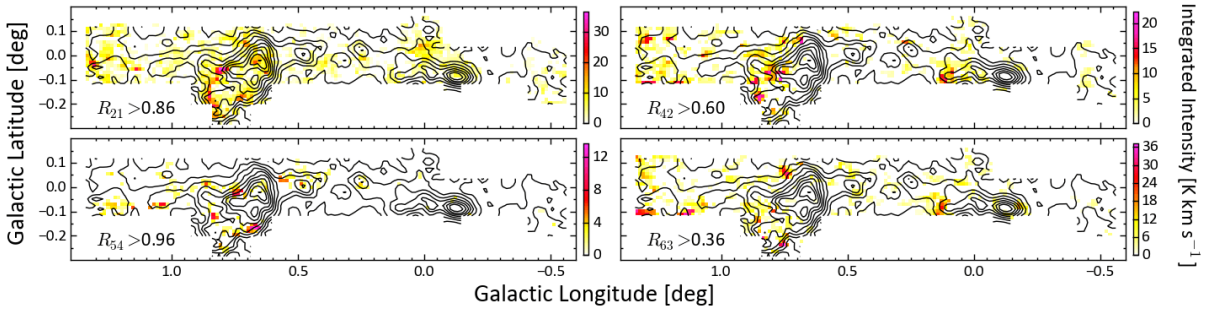

Fig. 10. Integrated intensity maps using only voxel where the intensity ratio is in the HR (color) overlaid on the distributions of the integrated intensity of the $(J, K) = (2, 2)$ line (contours). $T_{\rm mb}$ of the lower transitions are integrated.

3.6 Comparison with Data of Other Molecules

To grasp the physical condition and the environment of molecular gas, we compared our NH_3 intensity with some other molecular line data at same positions. Figure 11 shows scatter plots between $T_{\rm mb}$ of our NH_3 $(2, 2)$ and ^{13}CO (1–0) (Oka et al. 1998), CS (1–0), and CH_3OH (1_0–0_0) (Jones et al. 2013). NH_3 $(2, 2)$ is suitable for the comparison for the following reason; (1) contribution of both of the two temperature components (subsection 3.4), (2) the relative intensities of the hyperfine lines (to

the main line) are not strong (table 2). These data were summed into each 2 km s^{-1} velocity bin and the velocity range was cut to be $V_{\rm LSR} = -200$ to 200 km s^{-1} to fit our data. The spatial resolutions were also equalized to our data by smoothing. The original intensities of CS and CH_3OH were in the $T_{\rm A}^*$ scale. We converted them to the $T_{\rm mb}$ scale using $\eta_{\rm mb} \approx 0.43$ (Jones et al. 2013).

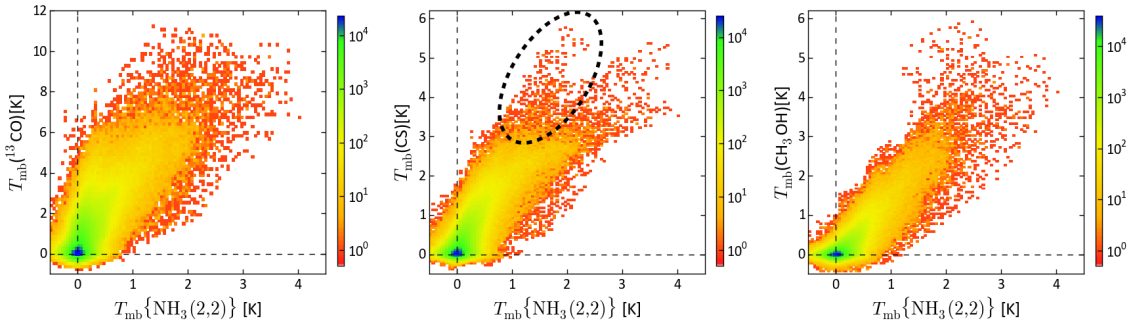

Fig. 11. $T_{\rm mb}$ scatter plot between NH_3 $(2,2)$ and other molecules in the observed area; *left*) ^{13}CO (1–0) (Oka et al. 1998), *middle*) CS (1–0) (Jones et al. 2013), *right*) CH_3OH (1_0–0_0) (Jones et al. 2013). The color indicates number of voxels.

In contrast to ^{13}CO, CS shows a better correlation with NH_3, which stemmed from the difference of the critical densities, $n_{\rm cr}$; NH_3 and CS ($J = 1$–0) trace dense molecular gas ($n_{\rm cr} > 10^4$ cm^{-3}), while ^{13}CO ($J = 1$–0) trace less dense molecular gas ($n_{\rm cr} = 10^{2\text{-}3}$ cm^{-3}). We found the intensity ratio of NH_3 to CS to be low in the majority of voxels of majority of the Sgr-A complex region (except of 20–km s^{-1} cloud, GCM$-0.13-0.08$). The voxels are located around $\{T_{\rm mb}({\rm NH_3}), T_{\rm mb}({\rm CS})\} = (1.8, 5.0)$ (enclosed by an ellipse in figure 11). This indicates a strong UV environment in the region, because CS is one of the molecules most tolerant to such a region (Drdla et al. 1989) while NH_3 is a UV-fragile molecule (Lee 1984). As NH_3, most of poly-atomic molecules such as CH_3OH, HNCO, and HC_3N are UV-fragile and weak around the Sgr-A complex region (Jones et al. 2012). Actually, CH_3OH shows the tightest correlation among them, which suggests similarity of creation/dissociation processes of NH_3 and CH_3OH. More detailed analysis will be shown in the forthcoming paper.

4 Summary

We carried out a survey of NH_3 $(J,K) = (1,1)$–$(6,6)$ in the major part of the CMZ with the Tsukuba 32-m telescope.

1. Significant emission (S/N > 3) of the NH_3 $(1,1)$–$(3,3)$ lines was simultaneously detected in 87% of the observed area (2323 out of 2655 positions). Among the 2323 positions, NH_3 $(4,4)$–$(6,6)$ were also detected with S/N > 3 at 1426, 1150 and 1359 positions, respectively.
2. The distribution and intensity of the NH_3 $(1,1)$ and $(2,2)$ data were consistent with the previous

survey data obtained with the Mopra 22-m telescope.

3. Some Boltzmann plots at representative points are shown. There seems to be two temperature components.
4. Typical intensity ratios among the NH_3 lines were $R_{21} = 0.71$, $R_{42} = 0.45$, $R_{54} = 0.65$, and $R_{63} = 0.17$. The distribution of R_{63} tends to be higher at outer parts of giant molecular clouds (GMCs) than at inner parts.

Acknowledgements. We are very grateful to the VLBI group of the GSI for licensing to use the 32-m telescope. The observations have been made under the agreement on the collaboration between the University of Tsukuba and the GSI. We thank Yuki SUKETA, Yoji MORI, Miyabi TSUBOKAWA, Kei-ichi ZEMPO, Shigeki TAKAOKA, Seika TAKAYANAGI, Takuya SUENAGA, Takao ICHIHARA, Shota FUKUOKA, Yuki OKURA, Sumire AOKI, Hirokazu MASUDA, Kazush KITAGAWA, Tsuguru RYU, Shoko KITAMOTO, Kazuki KOBAYASH, and Hiroki OKUTOMI for participating in the construction of the K-band observing system of the Tsukuba 32-m telescope. This work was supported in part by JSPS (Japan Society for the Promotion of Science) KAKENHI Grant Numbers 173400052, 17654042 and 20244011.

References

Ao, Y., Henkel, C., Menten, K., Requena-Torres, M.A., Stanke, T., Aalto, S., Mühle, S., & Mangum, J. 2013, A&A, 550, 125

Binney, J., Gerhard, O.E., Stark, A.A., Bally, J. & Uchida, K.I. 1991, MNRAS, 252, 210

Danby, G., Flower, D.R., Valiron, P., Schilke, P. & Walmsley, C.M. 1988, MNRAS, 235, 229

Drdla, K., Knapp, G.R., & Dishoeck, E.F. 1989, ApJ, 345, 815

de Pater, I., DeBoer D., Marley M., Freedman, R. & Young R. 2005, ICARUS, 173, 425

Flower, D.R., Pineau des Forêts, G. & Walmsley, C.M. 1995, A&A, 294, 815

Fukui, Y., et al. 2006, Science, 314, 106

Gordon, M.A. & Sorochenko, R.L., 2002, *Radio Recombination Lines*, Springer

Goldsmith, P.F. & Langer, W.D. 1999, ApJ, 517, 209

Goto, M., Usuda, T., Nagata, T., Geballe, T.R., McCall, B.J., Indriolo, N., Suto, H., Henning, T., Morong, C.P. & Oka, T. 2008, ApJ, 688, 306

Güsten, R., Walmsley, C.M. & Pauls, T. 1981, A&A, 103, 197

Hasegawa, T., Sato, F., Whiteoak, J.B. & Miyawaki, R. 1994, ApJ, 429, 77

Honma, M. et al. 2012, PASJ, 64, 136

Hüttemeister, S., Wilson, T.L., Bania, T.M. & Martín-Pintado, J. 1993, A&A, 280, 255

Jones, P.A., Burton, M.G., Cunningham, Requena-Torres, M.A., Menten, K.M., Schilke, P., Belloche, A., Leurini, S., Martín-Pintado, J., Ott, J. & Walsh, A.J. 2012, MNRAS, 419, 2961

Jones, P.A., Burton, M.G., Cunningham, M.R., Tothill, N.F. & Walsh, A.J. 2013, MNRAS, 433, 211

Koyama, K., et al. 2007, PASJ, 59, 245

Kukolich, S.G. 1967, Phys. Rev., 156, 83

Kutner, M.L. & Ulich, B.L. 1981, ApJ, 250, 341

Lee, L.C. 1984, ApJ, 282, 172

Lis, D.C., Phillips, T.G., Goldsmith, P.F. et al., 2010, ApJ, 521, L26

McGary, R.S. and Ho, P.T.P. 2002, ApJ, 577, 757

Menten, K.M., Wilson, R.W., Leurini, S. & Schilke, P. 2009, ApJ, 692, 47

Mills, E.A.C. & Morris, M.R. 2013, ApJ, 772, 105

Morris, M., Polish, N., Zuckerman, B., & Kaifu, N. 1983, ApJ, 88, 1228

Morris, M., & Serabyn, F. 1996, ARA&A, 34, 645

Nagayama, T., Omodaka, T., Handa, T., Iahak, H.B.H., Sawada, Y., Miyaji, T. & Koyama, Y. 2007, PASJ, 59, 869

Nagayama, T., Omodaka,T., Handa, T., Toujima, T., Sofue, Y., Sawada, T., Kobayashi, H. & Koyama, Y. 2009, PASJ, 61, 1023

Oka, T., Hasegawa, T., Sato, F., Tsuboi, M. & Miyazaki, A. 1998, ApJ, 118, 455

Pierce-Price, D., et al. 2000, ApJ, 545, L121

Purcell, C.R.., Longmore, S.N., Walsh, A.J., Whiting, M.T., Breen, S. L., Britton, T., Brooks, K. J., et al. 2012, MNRAS, 426, 1972

Riquelme, D., Amo-Baladrón, M.A., Martín-Pintado, J., Mauersberger, S., Martín, S., & Bronfman, L. 2013, A&A, 549, A36

Rodríguez-Fernández, N.J., Martín-Pintado, J. Fuente, A., de Vicente, P., Wilson, T.L. & Hüttemeister, S. 2001, A&A, 365, 174

Sakamoto, S. & Sunada, K. 2003, ApJ, 594, 340

Simmons, J. W. & Gordy, W. 1948, Phys. Rev., 73, 713

Tanaka, K., Oka, T., Nagai, M. & Kamegai, K. 2009, PASJ, 61, 461

Tsuboi, M., Handa, T. & Ukita, N. 1999, ApJS, 120, 1

Tsuboi, M., Miyazaki, A., and Uehara, K. 2015, PASJ, 67, 90

Ulich, B.J. & Haas, R.W. 1976, ApJS, 30, 247

Walmsley, C.M. & Ungerechts, H. 1983 A&A, 122, 164

Walsh, A.J., Breen, S.L., Britton, T., Brooks, K.J., Burton, M.G., et al. 2011, MNRAS, 416, 1764

Wilson, T.L., Ruf, K., Walmsley, C.M., Martín, R.N., Batrla, W. & Pauls, T.A. 1982 A&A, 115, 185

Wilson, T.L., Henkel, C. & Hüettemeister, S. 2006 A&A, 460, 533

Yusef-Zadeh, F., Muno, M., Wardle, M. & Lis, D.C. 2007, ApJ, 656, 847